Unsteady hydrodynamics of a full-scale tidal turbine operating in large wave conditions

Gabriel Thomas Scarlett[a], Brian Sellar[a], Ton van den Bremer[a,b], Ignazio Maria Viola[a,*]

[a]*School of Engineering, Institute for Energy Systems, The University of Edinburgh, Edinburgh, EH9 3DW*
[b]*Department of Engineering Science, University of Oxford, Oxford, OX1 3PJ*

Abstract

Tidal turbines operate in a highly unsteady environment, which causes large-amplitude load fluctuations to the rotor. This can result in dynamic and fatigue failures. Hence, it is critical that the unsteady loads are accurately predicted. A rotor's blade can experience stall delay, load hysteresis and dynamic stall. Yet, the significance of these effects for a full-scale axial-flow turbine are unclear. To investigate, we develop a simple model for the unsteady hydrodynamics of the rotor and consider field measurements of the onset flow. We find that when the rotor operates in large, yet realistic wave conditions, that the load cycle is governed by the waves, and the power and blade bending moments oscillate by half of their mean values. While the flow remains attached near the blade tip, dynamic stall occurs near the blade root, resulting in a twofold overshoot of the local lift coefficient compared to the static value. At the optimal tip-speed ratio, the difference between the unsteady loads computed with our model and a simple quasi-steady approximation is small. However, below the optimal tip-speed ratio, dynamic stall may occur over most of the blade, and the maximum peak loads can be twice those predicted with a quasi-steady approximation.

*Corresponding author
Email address: `I.M.Viola@ed.ac.uk` (Ignazio Maria Viola)

Keywords: tidal turbine hydrodynamics; fatigue loading; unsteady aerodynamics; blade-element momentum theory; dynamic stall; wave-induced loading

Nomenclature

a	Axial induction factor (-)
a'	Tangential induction factor (-)
A_R	Aspect ratio (-)
B	Geometry constant (-)
b_1	Rotational constant (-)
b_2	Rotational constant (-)
c	Chord length (m)
C_L^p	Lift coefficient in attached flow (-)
C_C^u	Unsteady chordwise force coefficient (-)
C_D^u	Unsteady coefficient (-)
C_N^u	Unsteady normal force coefficient (-)
C_N^v	Vortex normal force coefficient (-)
C_D^{ind}	Induced drag coefficient (-)
C_D^{st}	Static drag coefficient (-)
C_D^{vis}	Viscous drag coefficient (-)
C_D	Drag coefficient (-)
C_L	Lift coefficient (-)
C_N	Normal force coefficient (-)
C_P	Power coefficient (-)
C_Q	Torque coefficient (-)
C_T	Thrust coefficient (-)
C_{D_0}	Zero lift drag coefficient (-)
C_D^{rot}	Rotational drag coefficient (-)
$C_{F_{Tan}}$	Tangential force coefficient (-)
C_{F_T}	Thrust force coefficient (-)
C_L^u	Unsteady lift coefficient (-)
C_L^c	Circulatory lift coefficient (-)
C_L^{nc}	Non-circulatory lift coefficient (-)
C_L^{rot}	Rotational lift coefficient (-)
C_{M_x}	Edgewise bending moment coefficient (-)
C_{M_y}	Root bending moment coefficient (-)
C_{N_α}	Linear normal force (lift) curve (-)
C_N^{rot}	Rotational normal force coefficient (-)
d	Water depth (m)
D_α	Lagged angle deficit (-)
D_{ff}	Lagged separation point deficit (-)
E_0	Chordwise force recovery constant (-)
f	Separation point (-)
f'	Lagged separation point (-)
f''	Lagged separation point (-)
f^{rot}	Rotational separation point (-)
F_D	Drag force per unit length (Nm^{-1})
F_L	Lift force per unit length (Nm^{-1})

F_T	Thrust force per unit length (Nm^{-1})
F_{Tan}	Tangential force per unit length (Nm^{-1})
K	Axial inflow parameter (-)
K'	Tangential inflow parameter (-)
k_r	Reduced frequency (-)
L	Aerodynamic loss factor (-)
L_2	Least squares error (-)
M_X	Edgewise bending moment (Nm)
M_Y	Root bending moment (Nm)
N_b	number of blades (-)
Q	Torque acting on actuator disc (Nm)
R	Blade tip radius (m)
$\dot{r}$	Reduced pitch rate constant (-)
r	Blade radial coordinate (m)
R_h	Blade hub radius (m)
s	Reduced time (-)
T	Thrust force acting on actuator disc (N)
t	Time (s)
T_r	Period of rotation (s)
T_v	Vortex time lag constant (-)
T_α	Angle time lag constant (-)
T_{vL}	Vortex transit time (-)
U_0	Freestream reference velocity (ms^{-1})
U_ψ	Tangential velocity to blade (ms^{-1})
U_x	Streamwise velocity (ms^{-1})
U_z	Depthwise velocity (ms^{-1})
V_x	Vortex shape function (-)
W	Relative inflow velocity (ms^{-1})
x	Horizontal Cartesian coordinate (m)
y	Horizontal Cartesian coordinate (m)
z	Vertical Cartesian coordinate (m)
z_0	Depth of rotor hub (m)
α	Angle of attack (rad)
α'	Lagged angle of attack (rad)
α^{rot}	Rotational angle of attack (rad)
α_0	Angle of zero lift (rad)
α_{cr}	Critical angle (rad)
α_{ds0}	Critical dynamic stall onset angle (rad)
α_{ds}	Angle of dynamic stall onset (rad)
α_{ss}	Angle of static stall (rad)
$\dot{\alpha}$	Pitch rate (rads^{-1})
α_0	Zero lift angle of attack (rad)
α_E	Equivalent angle of attack (rad)
β	Pitch angle (rad)
β_g	Geometrical pitch angle (rad)
β_p	Operational pitch angle (rad)
Δ_α^{rot}	Rotational angle shift (rad)

Δ_{α_1}	Stall angle shift (rad)
η	Chordwise force recovery factor
λ	Tip-speed ratio (-)
λ'_r	Local instantaneous tip-speed ratio (-)
Ω	Rotor rotational speed (rads^{-1})
Φ	Wagner' function (-)
ϕ	Flow angle (rad)
ψ	Azimuthal position of blade (rad)
ρ	Density of working fluid (kgm^{-3})
σ	Dummy time variable of integration (s)
σ'_r	Local solidity (-)
τ	Vortex transit time (-)
θ	Phase angle of blade (rad)
BEM	Blade element momentum
D-ADP	Divergent beam Acoustic Doppler Profiler
DS	Dynamic stall
EMEC	European Marine Energy Centre
LCOE	Levelised cost of energy
OSU	Ohio State University
ReDAPT	Reliable Data Acquisition Platform for Tidal
SB-ADP	Single-beam Acoustic Doppler Profiler
SWL	Still water level

1. Introduction

Tidal current energy extraction is approaching a state of commercial readiness. Six full scale tests have been completed at the European Marine Energy Centre (EMEC), as well as several others elsewhere [1]. To date, the Crown Estate have issued 17 leases for tidal current energy extraction in Scottish waters, 9 of which are in the Pentland Firth [1], which according to one estimate has an estimated maximum power output of 1.9 GW [2]. Yet, questions remain regarding the performance and long-term survivability of a horizontal axis tidal turbine rotor operating in a harsh marine environment [3].

The marine environment is inherently unsteady due to waves and turbulence. The rotation of the blade through the shear layer of the tidal current and the unsteady flow causes a time-dependent flow field which can lead to unsteady flow phenomena such as load hysteresis, stall delay and dynamic stall. Stall delay is a process whereby the angle of attack increases sufficiently rapidly so that separation is prevented beyond the static stall angle, which causes lift increases above the maximum static value. Dynamic stall (DS) is when unsteady separation and stall occurs, resulting in a hysteresis loop of the lift with the angle of attack. If the angle of attack becomes large enough, dynamic stall may induce vortex shedding from the leading-edge of the blade. The convecton of the leading-edge vortex over the blade surface can produce load overshoots of 100% or more above the quasi-steady value [4]. These effects compounded with rotational forces and velocities induced by the dynamic wake behind the rotor make for a highly unsteady operational environment.

A probability analysis from 2012 investigated the survivability of a horizontal axis tidal turbine rotor using data extrapolated from similarly rated wind turbines [5]. The study estimated the reliability of tidal turbine blades would result in one failure every two years per turbine. Technology developers continue to improve devices. However, it is difficult to know the current state of the technology since failure rate data for full-scale devices is commercially sensitive. Certification standards for tidal turbine blades state that the nominal probability of failure per year should be under 10^{-4} [6]. A lack of quantifiable data relating to fatigue and extreme loading could lead to over conservative designs being produced in order to meet the standards, which will impact the levelised cost of energy (LCOE) and the roll-out-rate of technology.

Milne *et al*. [7] carried out experiments on a scaled turbine in a towing tank. The turbine was towed at a uniform speed whilst oscillating the external carriage on which it was mounted, replicating the type of unsteadiness caused by waves and large scale turbulence. At lower tip-speed ratios, they showed that the flow was largely separated over the entire blade span, which for high frequency forcing caused the root bending moment coefficient to exceed the quasi-steady value by up to 25%. In a later study, Milne *et al*. [8] highlighted the key stages of DS occurring in the root bending moment hysteresis. Galloway *et al*. [9] tested the effects of a yaw misalignment and waves using a wave tank to generate linear waves. Results were compared using an in house blade-element momentum (BEM) code, which included the Boeing-Vertol DS model and a dynamic inflow correction. The experimental results showed that the median value of the root bending moment was exceeded by up to 175% during the presence of large waves. Comparison between the results and the model were mixed with better prediction achieved for cases without yaw. The authors concluded that the effect of DS was limited and, therefore, can be neglected in some cases, despite not making comparison with quasi-steady values. These results are not in agreement with Milne *et al* [8].

Other than the work of Milne *et al*. [8], no documentation of DS occurring on tidal turbine blades exists. Yet, it is known to occur on all type of horizontal-axis wind turbines where skewed flow, shear, turbulence or tower shadow effects are present [10]. Since tidal turbine blades will also experience these effects with the addition of waves, it is likely that dynamic stall occurs. In addition, the difference between the mean value and the steady state has yet to be quantified. Understanding the unsteady flow around the blade and the resulting unsteady loads is of paramount importance to improve the reliability of tidal turbines without over-engineering components and increasing the LCOE. Moreover, detailed knowledge of the unsteady loads will enable the development of novel technology to mitigate the fatigue loadings and enhance the durability of tidal turbines [11, 12].

The aim of this work is to answer the following research questions:

1. How significant are the unsteady effects of very large, realistic waves on the flow around and the loads on a tidal turbine blade?

2. How important is modelling the unsteady dynamics as opposed to using a simpler less computationally intensive quasi-steady approximation?

To answer these questions a model is developed which couples state-of-the-art BEM, DS and rotational augmentation models with velocity field measurements taken at the EMEC test site during the ReDAPT project [13]. The model is freely available for use and can be downloaded from our GitHub repository [14]. We find that waves induce unsteady load phenomena ranging from low amplitude hysteresis at the outer sections to highly non-linear overshoots near the blade root, the significance of which is discussed in detail.

This paper is laid out as follows. In Section 2 (Field data measurements), we discuss how the velocity field measurements were made. In Section 3 (Turbine specification), we introduce the specification of the tidal turbine used in the model. In Section 4 (Formulation of the model), the formulation of the model and the solution method are given in detail. In Section 5 (Validation of the model), the key components of the model are validated. In Section 6 (Theoretical considerations), some theoretical considerations are made regarding the expected performance of the rotor when the onset velocity is varied. In Section 7 (Case study), the flow sample is introduced and the unsteady characteristics investigated. In Section 8 (Results), the predicted loads, power and bending moments predicted by the model are presented and discussed. Finally, in Section 9 (Conclusions), the main outcomes from this work are summarised.

2. Field data measurements

Data used herein was acquired during field measurement campaigns conducted by the University of Edinburgh at the EMEC tidal test site during the ReDAPT project between 2011 and 2015. Environmental data acquired up to October 2014 is publicly available at the UKERC Energy Data Centre in an archival format [15].

Time series of the free surface elevation were acquired using a remotely operable, single-beam acoustic Doppler profiler (SB-ADP) installed on a prototype turbine. The SB-ADP was orientated in the vertical direction measuring a fixed point in space directly above the hub of the turbine. Depth profiles of velocity measurements were provided by seabed mounted divergent beam acoustic Doppler profilers (D-ADP) deployed on the port and starboard sides of the turbine, approximately in line with the rotor plane, and at a distance of 40 m from the turbine. Using the vertically orientated SB-ADP, sea surface elevation was inferred from amplitude backscatter measurements at a sample rate of 4 Hz using image processing techniques. Results have been validated against an industry standard wave-measurement technique which is fully discussed in Sellar *et al.* [16].

3. Turbine specification

The dimensions of a 3-bladed, 1 MW tidal turbine representative of the Tidal Generation Ltd. DEEPGEN IV device deployed at the EMEC test site during the ReDAPT project are used. Schematic views of the port and front sides of the turbine are shown in Figure 1. A Cartesian coordinate system is placed at the still water level (SWL). The freestream current velocity is in the x direction, y is the port side direction and z is the vertical coordinate positive above the SWL. A cylindrical coordinate system with origin at the hub describes the radial (r) position along the blade, which extends to tip ($R = 9$ m), and the azimuthal angle of the blade (ψ), which tracks the position of the blade as it rotates anti-clockwise from the z axis where $\psi = 0$. Also shown are the radius of the hub (R_h), the water depth (d) and the distance from the hub to the SWL (z_0).

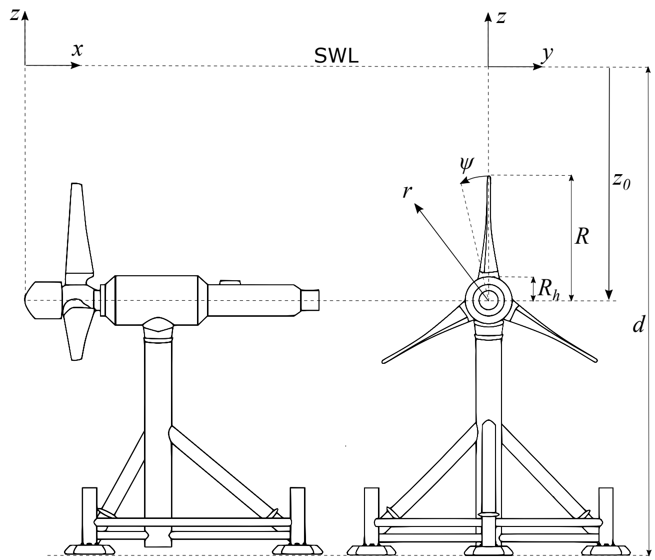

Figure 1: Schematic diagram of the tested tidal turbine (not to scale).

Chord (c) and geometrical twist (β_g) distributions along the blade span, which have been taken from Gretton [17], are shown in Figure 2.

The original blade profile has a non-uniform thickness and comprises of NACA 63-4XX geometries, where XX denotes the maximum camber thickness of each section in relation to c. To simplify we assume that all profiles have a uniform thickness, and to aid the modelling of DS we replace the NACA profile with a NREL profile since a large database of empirical dynamic stall parameters are availble for a series of NREL aerofoils [18]. The NREL S814 profile which has a thickness of 24% provides a similar power coefficient to the NACA 63-418 profile, so will be used throughout.

4. Formulation of the model

The model is split into three components: determination of the angle of attack, dynamic load coefficients and rotational augmentation, which are coupled

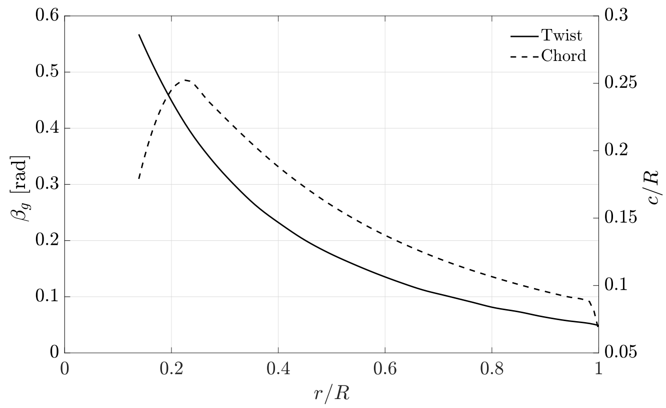

Figure 2: Blade chord and twist radial distribution (from [17]).

as detailed in this section.

4.1. Angle of attack time history

The velocity and force components acting on a blade section are computed as shown in Figure 3(a) and (b), respectively. The relative velocity (W) is the difference between the axial velocity $U_x(1-a)$ and the tangential velocity $U_\psi(1+a')$, where a and a' are the axial and tangential induction factors respectively, which account for velocities induced by the rotor wake. The angle of attack (α) is the angle that W makes with c, $\beta = \beta_g + \beta_p$ is the pitch angle which is measured between c and the rotor plane, where β_p is an operational pitch angle which may be applied to the blade. The flow angle is $\phi = \alpha + \beta$.

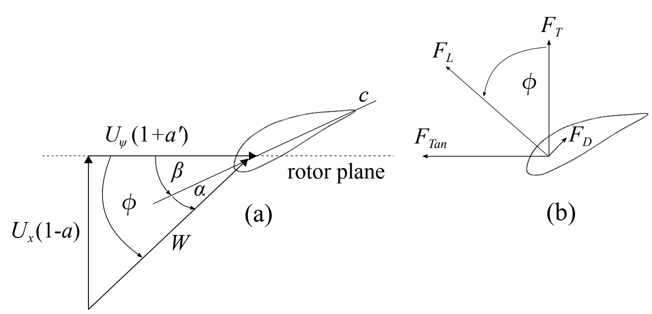

Figure 3: Blade section diagram showing (a) velocity components and (b) force components.

The sectional drag force (F_D) which is codirectional with W and the lift force (F_L) perpendicular to it are defined per unit length as

$$F_D = \frac{1}{2} C_D \rho W^2 c, \quad F_L = \frac{1}{2} C_L \rho W^2 c, \tag{1a, b}$$

where C_D and C_L are the sectional coefficients of drag and lift, respectively and ρ is the fluid density. The axial force known as thrust (F_T) is perpendicular to the rotor plane and is responsible for the blade bending around the y-axis known as root bending moment (M_Y). The tangential force (F_{Tan}) drives the turbine and causes bending around the x-axis referred to as edgewise bending moment (M_X). F_T and F_{Tan}, expressed in terms of F_D and F_L, are

$$F_T \equiv F_L \cos\phi + F_D \sin\phi, \tag{2}$$

$$F_{Tan} \equiv F_L \sin\phi - F_D \cos\phi, \tag{3}$$

which given in coefficient form are

$$C_{F_T} \equiv C_L \cos\phi + C_D \sin\phi, \tag{4}$$

$$C_{F_{Tan}} \equiv C_L \sin\phi - C_D \cos\phi. \tag{5}$$

Measured D-ADP velocity data is interpolated in time (t) and z to determine the horizonal velocity in x and the vertical velocity components incident on to each blade section for a given t. The z-coordinate of a blade section is $z_0 + r\sin(\psi - \theta)$, where θ is the phase lag from the leading blade, and $U_\psi = U_z \cos(\psi - \theta)$.

The induction factors are initially calculated in a quasi-steady manner for one revolution using the instantaneous velocities with static C_L and C_D values to solve the BEM equations [19]. The hydrodynamic forces are equated to the momentum rate of change acting on a blade annulus of width dr and position r on the blade, as shown in Figure 4.

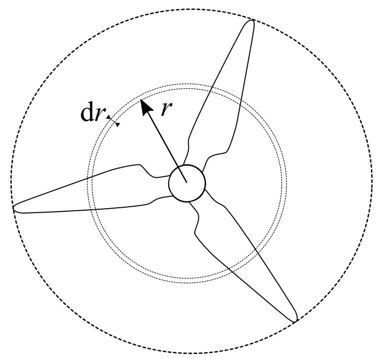

Figure 4: Incremental annulus swept out by a blade element.

The blade-element equations are defined as

$$\mathrm{d}T = N_b \frac{1}{2} \rho W^2 C_{F_T} c \, \mathrm{d}r, \tag{6}$$

$$\mathrm{d}Q = N_b \frac{1}{2} \rho W^2 C_{F_{Tan}} c \, \mathrm{d}r, \tag{7}$$

where $\mathrm{d}T$ and $\mathrm{d}Q$ are the incremental thrust and torque components acting on the annulus and N_b is the number of blades. The momentum balance equations for $\mathrm{d}T$ and $\mathrm{d}Q$ are

$$\mathrm{d}T = 4\pi r \rho U_0^2 (1-a) a L \, \mathrm{d}r, \tag{8}$$

$$\mathrm{d}Q = 4\pi r^3 \rho U_0 \Omega (1-a) a' L \, \mathrm{d}r, \tag{9}$$

where Ω is the rotational velocity of the rotor and L corrects for losses due to flow leakage at the extremities of the blade where a jump in tangential velocity occurs, causing the flow to roll up into a trailing helical vortex. L is determined using Prandtl's correction for both tip and hub losses [19]. Equations (8) and (9) are invalid for high induction ($a > 0.4$); in this region the empirical estimation of Glauret is used with the Buhl correction [20]. The blade-element and momentum equations are equated and rearranged to give the following implicit definitions for a and a':

$$a = \frac{K}{1+K}, \quad a' = \frac{K'}{1-K'}, \tag{10a, b}$$

where

$$K = \frac{\sigma' C_{F_T}}{4L\sin^2(\phi)}, \quad K' = \frac{\sigma' C_{F_{Tan}}}{4L\sin(\phi)\cos(\phi)}, \tag{11a, b}$$

and $\sigma' = N_b c/2\pi r$ is the local solidity. Equations (10)a and b are be solved iteratively. First, an initial guess is made for ϕ, from which β is deducted to give α, then the coresponding values of C_L and C_D are selected from look-up tables then, lastly, C_{F_T} and $C_{F_{Tan}}$ are determined. The present model uses the solution method of Ning [21], who utilises a residual equation to converge on ϕ rather than solving for both a and a'. This enables the use of a root finding algorithm which guarantees convergence. Using the geometrical definition for ϕ shown in Figure 3(a), the following residual equation is formed

$$R(\phi) = \frac{\sin(\phi)}{(1-a)} - \frac{\cos(\phi)}{\lambda_r'(1+a')}, \tag{12}$$

where $\lambda_r' = U_\psi/U_x$ is the instantaneous, local tip-speed ratio. The value of ϕ which satisfies $R(\phi) \leq 10^{-6}$ is determined and used in the following iteration. The process is repeated until $R(\phi) \leq 10^{-6}$. With the induction factors determined for each time step, these are time averaged over the rotational period (T_r). The solution to a at time t_i is

$$a = \frac{1}{T_r}\int_{t_i - T_r}^{t_i} a(t)\,\mathrm{d}t, \tag{13}$$

and we follow the same procedure for a'. Next, α time histories are calculated for each r as follows

$$\alpha(t) = \tan^{-1}\left(\frac{U_x(t)(1-a)}{U_\psi(t)(1+a')}\right) - \beta. \tag{14}$$

4.2. Dynamic load coefficients

The non-linear load coefficients are determined using the dynamic stall model of Sheng *et al*. [22]. This DS model is based on the 3rd generation dynamic stall model of Beddoes [23], but with a number of adaptations made to achieve better prediction at the lower Mach numbers associated with wind turbines. We modify the model to account for the effects of blade rotation and use the definition for the unsteady drag coefficient given by Hansen *et al*. [24].

The total unsteady load response comprises of three elements: attached flow, trailing edge separation and leading edge vortex shedding, which we will now discuss.

4.2.1. Load response in attached flow

The linear lift coefficient comprises of both circulatory and non-circulatory components. The latter accounts for flow acceleration effects, and the former for circulation around the foil and vorticity shed into the wake. Theodorsen [25] showed that this cirulatory component introduces a phase lag and amplitude reduction in the lift from the quasi-steady value. Sheng *et al.* determine the linear solution using a method developed by Beddoes [23], who considers compressibility effects. However, for a tidal turbine the maximum Mach number is approximately 0.03, which occurs at the blade tip and is an order of magnitude less than the compressible range. Thus the attached loads are determined using the incompressible time domain solution of Wagner [26], who gives the circulatory lift coefficient (C_L^c) due to a unit step change in α. The C_L^c time history for a number of arbitrary unit step changes in α is determined by superposition through the Duhamel integral as follows:

$$C_L^c = 2\pi\alpha_E, \tag{15}$$

where the equivalent angle of attack that lags the physical α is

$$\alpha_E = \alpha(0)\Phi(s) + \int_0^s \frac{\mathrm{d}\alpha(\sigma)}{\mathrm{d}s}\Phi(s-\sigma)\mathrm{d}\sigma, \tag{16}$$

$\Phi(s)$ is the Wagner function, its argument $s = 2U_0t/c$ is the non-dimensional reduced time, U_0 is the freestream velocity and σ is a dummy time variable of integration. Wagner does not give a convenient analytical solution to $\Phi(s)$. Therefore, the following exponential approximation given by Jones [27] is used

$$\Phi(s) \approx 1 - 0.1652e^{-0.0455s} - 0.335e^{-0.3s}. \tag{17}$$

The non-circulatory coefficient (C_L^{nc}), i.e. the added mass, is treated outside of the Duhamel integral. For this term we use the approximation given by Hansen *et al.* [24], where

$$C_L^{nc} = \frac{\pi c \dot{\alpha}}{2U_0}, \tag{18}$$

where

$$\dot{\alpha} = \frac{\mathrm{d}\alpha}{\mathrm{d}t}. \tag{19}$$

Then the full lift coefficient in attached flow is

$$C_L^p = C_L^c + C_L^{nc}. \tag{20}$$

For an arbitrary α forcing, (15) and (18) are determined numerically.

4.2.2. Load response in separated flow

The first part of the non-linear solution is the load response in separated flow. To quantify this, Kirchhoff theory [28, p. 170] is used, which relates the position of the trailing-edge separation point to the static normal force coefficient C_N. The separation point coordinate x is normalised by the chord length (c) giving a non-dimensional separation point f, as illustrated in Figure 5. When the boundary layer is fully attached, $f = 1$, and when fully separated, $f = 0$.

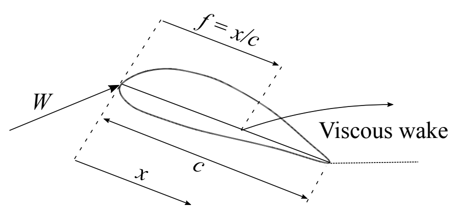

Figure 5: Trailing-edge separation point described by Kirchhoff flow past a flat plate.

The relationship between C_N, α and f is

$$C_N = C_{N_\alpha}(\alpha - \alpha_0)\Big(\frac{1+\sqrt{f}}{2}\Big)^2, \tag{21}$$

where $C_{N_\alpha} = \frac{\mathrm{d}C_N}{\mathrm{d}\alpha}|_{\alpha_0}$ is the slope evaluated at the angle of zero lift (α_0). Equation (21) is rearranged to solve for f using static C_N wind tunnel test data [29]. Then, f is determined for any α using a look-up table. Under unsteady conditions, boundary layer separation is delayed to a higher value of α. We can model this angle (α') as a first-order lag in the s domain, namely

$$\frac{\mathrm{d}\alpha'}{\mathrm{d}s} = -\frac{(\alpha' - \alpha)}{T_\alpha}, \tag{22}$$

where T_α is an empirical non-dimensional time constant describing the angle of attack delay. The solution for α' is

$$\alpha' = \alpha(1 - \exp(-s/T_\alpha)). \tag{23}$$

For arbitrary forcing the exponential decay is modelled numerically with a deficit function D_α such that

$$\alpha' = \alpha - D_\alpha. \tag{24}$$

Then numerically

$$D_{\alpha_j} = D_{\alpha_{j-1}} \quad \exp\left(\frac{\Delta s}{T_\alpha}\right) + (\alpha_j - \alpha_{j-1}) \quad \exp\left(\frac{\Delta s}{2T_\alpha}\right), \tag{25}$$

where j denotes the current time step. With α' determined, the dynamic separation point f' is found using the look-up table and replacing α as follows

$$f'(\alpha) = f(\alpha' - \Delta\alpha_1), \tag{26}$$

where $\Delta\alpha_1$ is a shift delay from the static stall angle (α_{ss}).

4.2.3. Dynamic stall onset

The critical dynamic stall onset angle is defined

$$\alpha_{cr} = \begin{cases} \alpha_{ds0}, & \dot{r} \geq \dot{r_0} \\ \alpha_{ss} + (\alpha_{ds0} - \alpha_{ss})\frac{\dot{r}}{\dot{r_0}}, & \dot{r} < \dot{r_0}, \end{cases} \tag{27}$$

where $\dot{r} = \dot{\alpha}c/2U_0$, is the reduced pitch rate, $\dot{r_0}$ is the value of $\dot{r}$ above which α_{cr} increases linearly and α_{ds0} is the constant dynamic stall onset angle.

The shift delay from α_{ss} is evaluated is evaluated in a similar manner

$$\Delta\alpha_1 = \begin{cases} \alpha_{ds0} - \alpha_{ss}, & \dot{r} \geq \dot{r_0} \\ (\alpha_{ds0} - \alpha_{ss})\frac{\dot{r}}{\dot{r_0}}, & \dot{r} < \dot{r_0}. \end{cases} \tag{28}$$

Then stall onset occurs when

$$\alpha' \geq \alpha_{cr}. \tag{29}$$

4.2.4. Dynamic stall load response

After the onset of dynamic stall an additional lag in the separation point occurs, as the leading edge vortex forms causing an additional load overshoot. As with α' a first-order lag is implemented to determine the dynamic separation point (f'')

$$\frac{\mathrm{d}f''}{\mathrm{d}s} = -\frac{(f'' - f')}{T_v}, \tag{30}$$

where T_v is the non-dimensional vortex time constant which includes both the formation and convection time. The solution is again modelled with a deficit function (D_{ff}) which describes the lag due to the dynamic vortex as

$$f'' = f' - D_{ff}, \tag{31}$$

with D_{ff} solved numerically as

$$D_{ff_j} = D_{f_{j-1}} \quad \exp\left(\frac{\Delta s}{T_v}\right) + (f'_j - f'_{j-1}) \quad \exp\left(\frac{\Delta s}{2T_v}\right). \tag{32}$$

Vortex shedding follows the method of Beddoes [23], which uses a vortex shape function (V_x) defined as follows:

$$V_x = \begin{cases} \sin^{3/2}\left(\frac{\pi\tau}{2T_v}\right), & 0 < \tau \leq T_v \\ \\ \cos^2\left(\frac{\pi(\tau - T_v)}{T_{vL}}\right), & T_v < \tau, \end{cases} \tag{33}$$

where τ is the non-dimensional vortex passage time (scaled the same as s) which increases from zero at the onset of dynamic stall, and T_{vL} is the speed of the vortex convection. Subsequent vortex shedding occurs for $\tau > T_v$ until the foil starts pitching down ($\dot{r} < 0$) and V_x is set to zero. The additional lift contribution due to vortex shedding is then computed as the difference between the delayed and the static separation points multiplied by the shape function

$$C_N^v = B(f' - f)V_x, \tag{34}$$

where B is a constant dependent on aerofoil geometry.

4.2.5. Non-linear force coefficients

The final expression for the normal force coefficient C_N is

$$C_N^u = C_N^c\Big(\frac{1+\sqrt{f''}}{2}\Big)^2 + C_N^{nc} + C_N^v. \tag{35}$$

The expression for the chordwise force coefficient is

$$C_C^u = \eta C_{N\alpha}(\alpha_E - \alpha_0)^2(\sqrt{f'} - E_0), \tag{36}$$

which has no contribution from the vortex. The parameters η and E_0 are both dependent on the sectional geometry. The lift coefficient is then

$$C_L^u = C_N^u \cos(\alpha) + C_C^u \sin(\alpha). \tag{37}$$

In the model of Sheng *et al*. [30] the drag coefficient is defined as

$$C_D^u = C_N^u \sin(\alpha) - C_C^u \cos(\alpha) + C_{D0}, \tag{38}$$

where C_{D0} is the drag coefficient at α_0. However, this definition does not bound C_D^u to the static drag curve. Therefore, we instead use the definition provided by Hansen *et al*. [31], which is expressed as three terms

$$C_D^u = C_D^{st} + C_D^{ind} + C_D^{vis}, \tag{39}$$

where

$$C_D^{ind} = C_L^u(\alpha - \alpha_E), \tag{40}$$

and

$$C_D^{vis} = (C_D^{st} - C_{D0})\Big(\frac{1+\sqrt{f''}}{2}\Big)^2 - \Big(\frac{1+\sqrt{f(\alpha_E)}}{2}\Big)^2, \tag{41}$$

where C_D^{st} is the static drag coefficient determined from wind tunnel test data [29]. The three terms on the right hand side of (39) are the static, induced and viscous components, respectively. C_D^{vis} is zero when the flow remains attached since $f'' = f(\alpha_E)$, and under near steady conditions $C_D^{ind} \to 0$ as $\alpha_E \to \alpha$.

The empirical parameters for the NREL S814 are shown in Table 1. They are taken from [18], with slight modifications made using the Ohio State University (OSU) wind tunnel test data [29].

Table 1: Table of empirical parameters for the NREL S814.

α_{ds0}	0.2426
α_{ss}	0.2007
α_0	-0.0573
C_{D0}	0.01
$C_{N\alpha}$	6.267
E_0	0.1
η	1
$\dot{r}_0$	0
T_α	6.33
T_v	4
T_{vL}	6
B	0.5
b_1	0.5
b_2	0.5

4.3. Rotational augmentation

Rotation of the blades induces a centrifugal force which causes a spanwise flow and an apparent Coriolis force which accelerates the flow towards the trailing edge. These effects reduce the adverse pressure gradient to promote flow reattachment and delay separation, which in turn leads to lift augmentation from the stationary value [32]. Modelling techniques of this phenomenon have had mixed success. The NREL Phase VI test investigated the effects of both unsteadiness and rotation on a 10 m diameter wind turbine employing NREL S809 profiles [33]. The study found that for inboard blade sections both lift and drag force are augmented compared to a non-rotating blade. However, conversely, for outer blade sections, both lift and drag are reduced. Modeling this behavior is a challenge. Breton *et al*. [34] tested the prediction capabilities of a number of rotational augmentation models to predict the NREL Phase VI test data. Their study determined that none of the models could satisfactorily predict C_L and C_D across the entire blade span, and that only the Lindenburg model [35] successfully captured a reduction in C_L at the outer sections. The Lindenburg model is well-suited to combination with the DS model since both use the separation point parameter f. To this end, we implement Lindenburg's model and combine it with the DS implementation.

The expression for the rotational lift coefficient is

$$C_L^{rot} = C_L + \frac{b_1 c}{r} \cos^2(\phi)((1-f)^2 \cos(\alpha^{rot}) + b_2 \cos(\alpha^{rot} - \alpha_0)), \tag{42}$$

where b_1 and b_2 are empirical coefficients tuned to the NREL S809 using data from the NREL VI tests, which we will use in our model, and $\alpha^{rot} = \alpha + \Delta\alpha^{rot}$ is the equivalent rotational angle of attack with the following shift applied

$$\Delta\alpha^{rot} = \frac{b_1 b_2 c}{2\pi r} \cos^2(\phi). \tag{43}$$

At the outer sections ($r \geq 0.8R$) where a reduction from the non-rotating lift and drag values occur C_L^{rot} is given as

$$C_L^{rot} = C_L - \Big(\frac{\cos^2(\phi) \exp(-1.5 A_R) C_L (C_{N_\alpha}(\alpha - \alpha_0) - 1)}{C_{N_\alpha}(\alpha - \alpha_0)}\Big), \tag{44}$$

where A_R is the aspect ratio of the outboard blade element. Lindenburg defines the rotational drag coefficient (C_D^{rot}) at all sections as

$$C_D^{rot} = C_D \frac{b_1 c}{r} \cos^2(\phi)(1-f)^2 \sin(\alpha^{rot}), \tag{45}$$

The NREL phase VI results clearly show a reduction in the drag coefficient at the outer sections of the blade [33]. Therefore the present model will assume for $r \geq 0.8R$, that $C_D^{rot} = C_D$ to avoid an over-prediction.

Using Lindenburg's theory we modify the DS model to superimpose rotational augmentation on both C_L^u and C_D^u. This is implemented by first modifying the separation point such that it is also a function of r by determining C_N^{rot} for each section and replacing C_N in (21) to determine f^{rot} for each r. Then a look-up table is used to determine f^{rot} in terms of both α and r. Then f in (26) and (34) is replaced with f^{rot}. Lastly, we apply the angle shift given by

(43) to both the static stall angle $\alpha_{ss}^{rot} = \alpha_{ss} + \Delta\alpha^{rot}$, and the critical dynamic stall onset angle $\alpha_{ds0}^{rot} = \alpha_{ds0} + \Delta\alpha^{rot}$.

4.4. Coupled blade-element momentum model

The unsteady, rotational load coefficients are coupled with the BEM model to investigate the effect on the induction factors; something which has not previously been reported in the literature.

Due to hysteresis and non-linearities, $C_L^u(t)$ and $C_D^u(t)$ are non-unique for a given α. This is a problem for the BEM model which requires predefined values of C_L and C_D for a given α. To accomodate this, $C_L^u(t)$ and $C_D^u(t)$ are collected from the previous time steps over the period of revolution, sorted into α bins, and the mean value calculated for each bin. A smoothing spline is then applied to the points to achieve a continuous set of values. After this the Viterna deep stall extrapolation [36] is applied. This extends the coefficients α range between $-\pi$ and π, which is a numerical requirement of the BEM model. The look-up tables, containing unique values of $C_L^u(\alpha)$ and $C_D^u(\alpha)$ for each r are then passed to the BEM model. New values of a and a' are determined and fed back into the numerical model, coupling the unsteady response with the induction factors. The solution is iterated until the sum of the squares error over r, $L_2 \leq 10^{-6}$, where

$$L_2 = \sum_{r=R_h}^{R} (\Delta a)^2 , \tag{46}$$

here Δa is the difference between the current and the previous value.

A flow diagram is shown in Figure 6 which illustrates the key stages and logic of the numerical model. The initial conditions first determine U_x and U_ψ as previously described, then solve a and a' for the first rotation using the static coefficients. After this α and the subsequent unsteady, rotational coefficients are calculated. The coefficients are then transformed into $C_L^u(\alpha)$ and $C_D^u(\alpha)$, enabling the BEM model to solve the new induction factors at each time step, which are then time averaged and fed back into the coupled model until convergence is satisfied. After which time increases by an increment Δt, and the converged solution becomes the new initial condition. The process continues until the time history is complete.

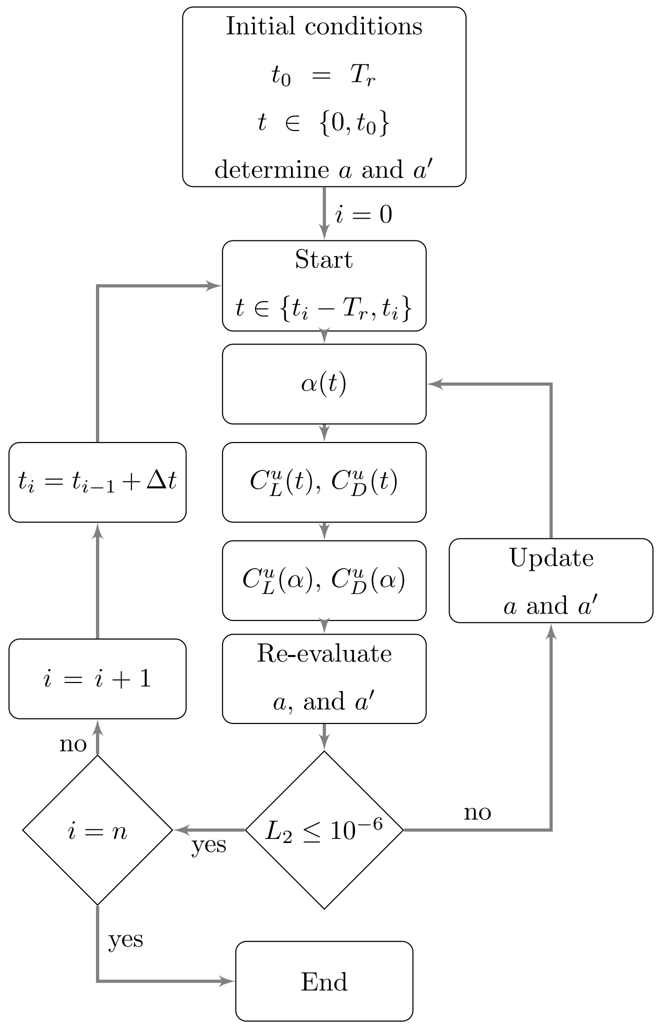

Figure 6: Process diagram of the coupled model.

5. Validation of the model

We validated the key components of the numerical model. First the BEM implementation is used to predict values of power (C_P) and thrust (C_T) coefficients, respectively for a range of tip-speed ratios ($\lambda = \Omega R/U_0$) $\in \{0.5, 8\}$, which are compared to those predicted using AeroDyn, an opensource aerodynamic software developed by NREL, which also uses the theoretical implementation of Ning *et al*. [37]. The turbine employs uniform thickness NREL S814 profiles at each section, the flow is steady with a current velocity of 2.77 ms^{-1}, the rotor is normal to the flow and $\beta_p = 0$. The results are shown in Figures 7(a) and 7(b) for C_P and C_T, respectively. The predicted values of C_P are in very good agreement with that of AeroDyn up until $\lambda = 5$, after which the value is slightly under predicted compared to AeroDyn, although both have similarly decreasing slopes. The predicted values of C_T agree well across the full range, apart from a slight over prediction for $\lambda \in \{4, 5\}$. These results verify that the BEM implementation is performing as expected.

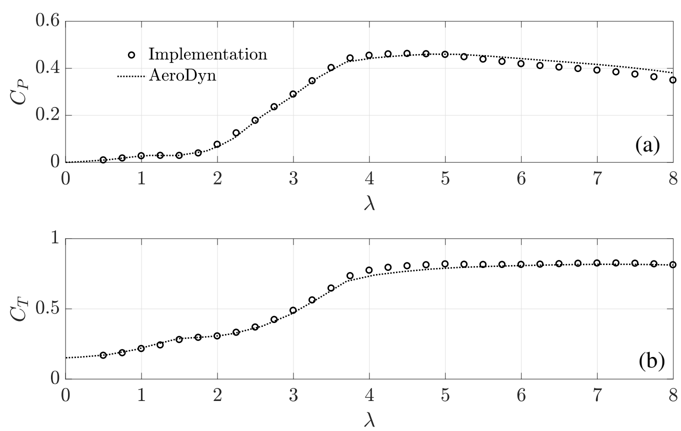

Figure 7: Power (a) and thrust (b) coefficient performance curves for a turbine operating in steady conditions.

Next, the predictive capabilities of the DS model are tested. The relationship between C_L and α for the S814 aerofoil is shown in Figure 8 for a number of cases. Empirical values from the OSU wind tunnel tests are shown for the measured static and dynamic cases [29]. Predicted values are shown for the dynamic case, and for both the static and dynamic cases with the effect of rotational augmentation. The forcing is $\alpha = 13.8^\circ + 10.75^\circ \sin(\omega t)$, the reduced frequency, defined $k_r = 2\pi\omega c/W$ is 0.091 and for the rotational case, $r = 0.47R$.

The dynamic model predicts the value of C_L when pitching positively from around $3°$ to $18°$ very well compared to the measured dynamic data, and the shape of the load hysteresis matches qualitatively.

The model predicts the increase in lift at around $18°$ caused by vortex shedding, as well as the partial recovery from stall at around $23°$ due to a secondary vortex being shed. During the return from stall, when α is decreasing the model overpredicts C_L. Prediction in this region could be improved by using an additional return from stall model which Sheng *et al.* discuss [22]. However, implementation for the type of arbitrary α history caused by the wave group shown in Figure 11 would be challenging, and is therefore, not included.

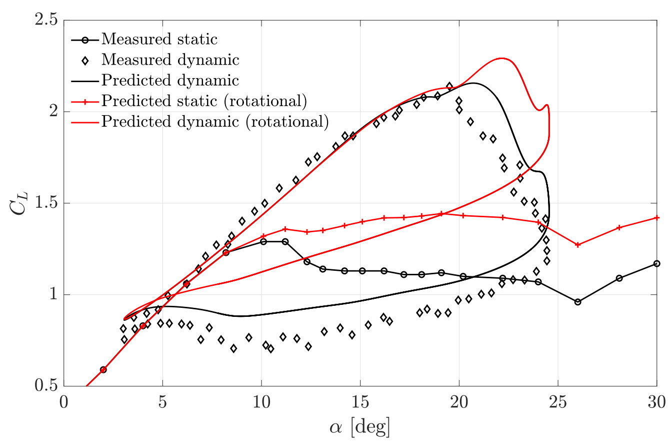

Figure 8: Lift coefficient as a function of angle of attack for static and dynamic conditions, with and without the effect of rotation.

The modification made to combine the effects of DS with rotational augmentation cannot easily be validated since no dynamic rotational data exists for the NREL S814. However, a qualitative comparison can be made using the NREL Phase VI experimental data for the S809. Figure 9 which has been reproduced from Guntur *et al.* [38] shows the lift coefficient curve for a pitching NREL S809 foil for the rotational and non rotational cases. Here k_r is 0.1 and the location along the blade is also $0.47R$. The difference between the non-rotational and rotational curves for the S809 matches qualitatively with the difference between modelled dynamic and dynamic rotational curves for the S814 shown in Figure 8. The rotating foil generates a larger value of C_L, with a prominent increase due to vortex shedding visible from 17° to 19°. During the return from stall the value of C_L is approximately 50% greater for the rotational case. This confirms that dynamic lift is enhanced by rotational augmentation, and the severity, in terms of the area enclosed by the hysteresis is reduced.

The DS model agrees well quantitatively for increasing α, and captures qualitatively the hysteresis shape and transient vortex shedding which characterises dynamic stall. The qualitative agreement with the rotational data for the NREL S809 suggests that the modification is sufficient to superimpose the effect of rotational augmentation on the unsteady loading.

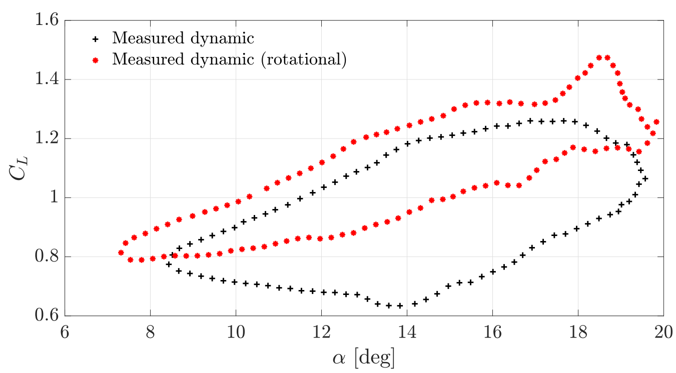

Figure 9: Unsteady lift coefficient with angle of attack for the NREL S809 aerofoil for a rotating and non-rotating aerofoil (reproduced from [38]).

6. Theoretical considerations

We review and compare the difference in power (P) and C_P of a rotor operating at variable and fixed speed. A variable speed rotor adjusts its angular velocity Ω whilst keeping its tip-speed ratio λ constant, whereas a fixed speed rotor keeps Ω constant and λ varies. We consider $U_x \in \{1.5, 4.5\}$ ms^{-1}, a variable speed with $\lambda = 4.5$ and a fixed speed with $\Omega = 1.25$ rads^{-1}. To enable a clear interpretation of the results, we consider $C_D = 0$, $C_L = 2\pi\alpha$, we take a

constant (0.3) and $a' = 0$, for all r. The results are shown in Figure 10. Observing the computed $\lambda =$ constant values we find that by varying Ω according to the onset velocity that $P \propto U_x^3$ and C_P remains constant. On the other hand, by keeping Ω fixed, as shown in Figure 10(a) $P \propto U_x^{2.71}$, which is a fit specific to these conditions. Even when such a large range of flow velocity is considered, the difference between the two curves is marginal. This important result suggests that if C_p is defined as in (47) then the mean C_p is almost constant for any unsteady onset flow condition, even if the rotational speed is not adjusted to keep the optimal tip speed.

$$C_p = \frac{P}{\frac{1}{2}\rho\langle U_x^3\rangle A}, \tag{47}$$

where P is the power extracted, ρ the water density, A the area swept by the rotor and the angle brackets indicate the double average over Δt and A.

We might have erroneously expected that, by fixing Ω, $P \propto U_x^2$.

For a turbine with three blades the power is defined as

$$P = \Omega \sum_{j=1}^{3} Q_j, \tag{48}$$

where j denotes the blade and Q_j is the torque on blade j, which is

$$Q_j = \int_0^R F_{tan} r \,\mathrm{d}r. \tag{49}$$

From Equation 3

$$F_{tan} = \frac{1}{2} C_L \sin(\phi) \rho W^2 c, \tag{50}$$

therefore it would seem that $P \propto W^2 \propto U_x^2$. However, since $C_L \propto \alpha \propto U_x$, then $P \propto U_x^3$.

From Figure 10(b) we observe that keeping Ω constant, the rotor does not operate constantly at the optimal λ, resulting in a marginal loss in performance, which is the reason why we find $P \propto U_x^{2.71}$. This is important for high frequency flow fluctuations where it would not be possible to match λ to $U_x(t)$ by constantly varying Ω.

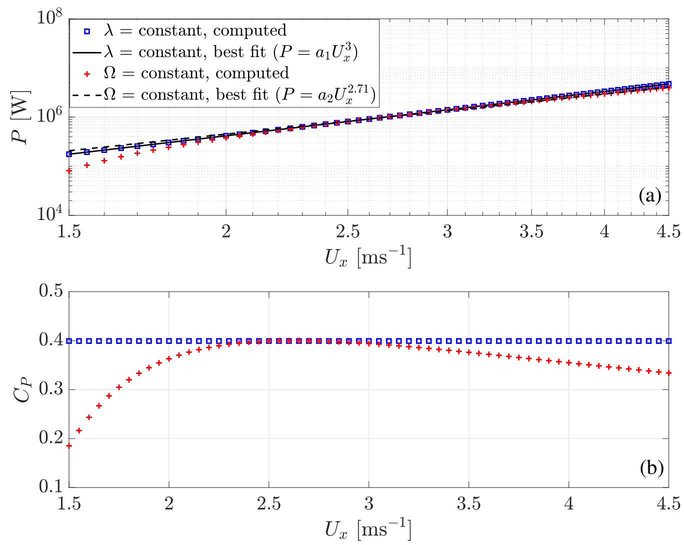

Figure 10: Comparison of variable and fixed speed rotor operation with freestream velocity: (a) power for varied rotational speed, (b) power generated for fixed speed rotation (c) power coefficient for varied rotational speed and (d) power coefficient for fixed speed rotation.

7. Case study

In this study, a 256 s flow sample measured during a flood tide at EMEC on the 22nd of November 2014 is used. The sample was selected on the basis of it containing an energetic wave train and to investigate the unsteady hydrodynamic response of the rotor. The waves, which originate from the North Sea, are opposing the current. The free surface elevation (η) is measured at a fixed point in space directly above the turbine nacelle. The η time history is shown over 250 s in Figure 11(a). The significant wave height from the sample is 4.2 m and the maximum wave height observed is approximately 5 m with a wave period of 10 s. The wave steepness, defined as the product of wave amplitude and wave number is approximately 0.17, indicating that the wave is weakly non-linear. The power spectral density (S) of η, shown in Figure 11(b), confirms that the energy contained within this wave group is centred around 0.095 Hz.

Streamwise (U_x) and depthwise (U_z) velocities are measured from the bed to the SWL in 1 m increments at a sampling frequency of 0.5 Hz, where $d = 45$ m,

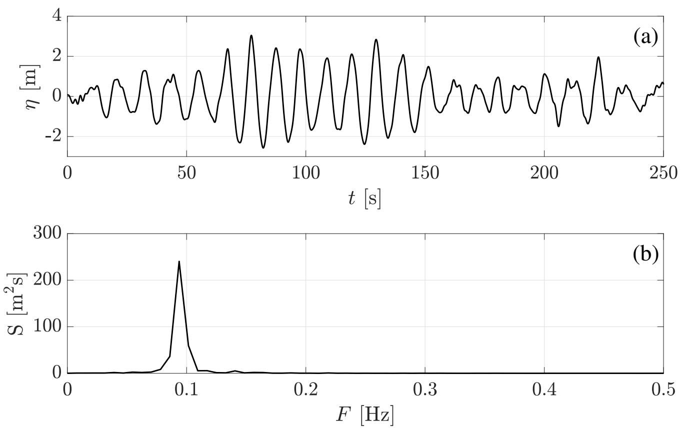

Figure 11: Free surface elevation (a) time history and (b) power spectrum density.

$z_0 = -27$ m and the rotor operates at $z \in -18, -36$. The location of the D-ADP is approximately $y = -40$ m, which is deemed far enough away from the rotor wake and tower to be measuring the freestream [39]. Thus, velocity readings incorporate the effects of waves, turbulence and the shear profile, but not velocities induced by the wake or the support structure of the turbine. Tower shadow effects due to the support structure are neglected in this study since our preliminary study showed that the load amplitude caused was an order of magnitude less than that due to waves approximately 3.6 m high with 7.7 s periods [40].

The time averaged U_x depth profile from 3 m above the bed ($z = -42$ m) to the SWL is shown in Figure 12. The current velocity depth profile of U_x for $z \in \{-18, -36\}$ follows a power law with exponent 0.162, with a hub velocity of 2.70 ms^{-1}. The power spectral density of U_x is shown in Figure 13(a) for the blade tip at $z = -18$ m, $z_0 = -27$ m , and $z_0 = -36$ m. The peak frequency in the velocity spectrum at both $z = -18$ m and $z = -27$ m corresponds to the 0.095 Hz value found in the η spectrum. As the depth increases from $z = -18$ m to $z = -27$ m, the energy peak associated with the wave decays by about 80%, and at $z = -36$ m the value has decreased by roughly 95%. The power spectral density of U_z is shown in Figure 13(b). As with U_x, the energy decreases with

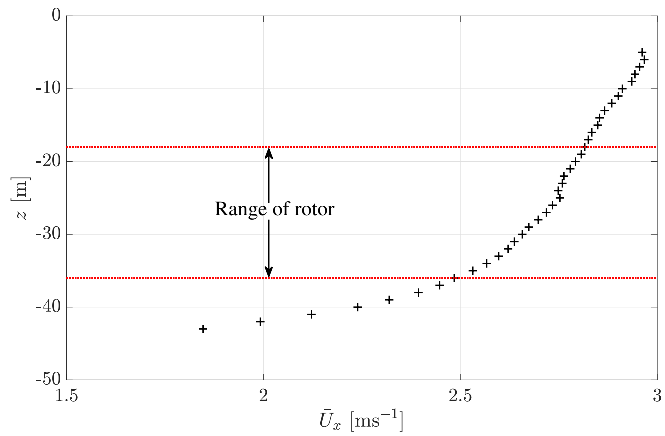

Figure 12: Time averaged depth profile of the streamwise velocity.

increasing depth and has a peak centred at the wave frequency.

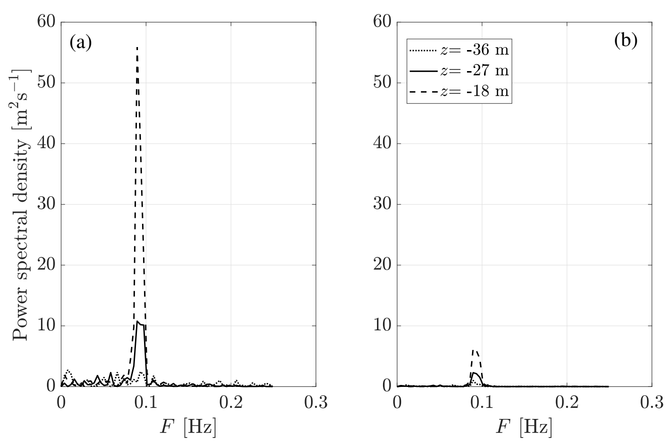

Figure 13: Power spectral density of (a) the streamwise velocity and (b) the vertical velocity encountered at the minimum ($z = -18$ m), hub ($z = -27$ m) and maximum ($z = -36$ m) depth ranges of the turbine blade.

The fact that power spectral density of both U_x and U_z have peaks centred around the peak wave frequency confirms that the waves recorded above the turbine correlate well with the measurements taken $y = -40$ m away from the hub.

8. Results

8.1. Power and thrust

The magnitude of U_x averaged over the swept area and the sample time period of 256 s is $\langle U_x \rangle = 2.72$ ms^{-1}, while the mean of the square $\sqrt{\langle U_x^2 \rangle} = 2.74$ ms^{-1} and the mean of the cube $\sqrt[3]{\langle U_x^3 \rangle} = 2.77$ ms^{-1}. The latter velocity is used for the steady simulation and to nondimensionalise forces, torque and power. The operating parameters λ and β_p, which yield a maximum C_P in a steady current with $U_0 = 2.77$ ms^{-1} are determined using the BEM model with static coefficients corrected for rotation. C_P is simulated for $\lambda \in \{3, 6\}$ in steps of 0.1, combined with $\beta_p \in \{-10°, 10°\}$ in steps of 0.1°. A peak $C_P = 0.47$ was found to occur for $\lambda = 4.5$ and $\beta_p = 0.1°$, with $C_T = 0.81$. All subsequent simulations are carried out using these operating parameters.

Values for C_P and C_T for both steady and unsteady conditions are shown in Figure 14 for ten rotational periods ($T_r = 4.5$ s). Unsteady fluctuations are clearly dominated by the period of the wave, with no discernible contribution from the rotational period. These fluctuations were found to exceed the steady value by up to 48% and 25% for C_P and C_T, respectively. Comparing the mean value of the unsteady time history with the steady value reveals a power decrease of 3% and a thrust decrease of 3% from the steady-state. Here, the steady state result is computed with the same model used for the unsteady case but using a steady uniform onset flow.

To investigate what causes the mean power coefficient to decrease, we performed additional simulations where we gradually simplified the model. Firstly, we perform a quasi-steady simulation without accounting for the load hysteresis, stall delay and dynamic stall, and using the static force coefficients from wind tunnel tests. Then, we use linear force coefficients, i.e. $C_L = 2\pi(\alpha - \alpha_0)$ and $C_D = 0$. Finally, we perform a steady simulation in an ideal, steady, uniform flow with $U_0 = \sqrt[3]{\langle U_x^3 \rangle} = 2.77$ ms^{-1}. In total we found a 7% reduction from this latter steady ideal case to the fully unsteady mean value shown in Figure 14(a). This 7% loss can be broken down as follows. Firstly, the effect of an unsteady onset flow leads to a loss of 0.5%. As discussed in the Theoretical considerations (Section 6), this can be avoided by operating the turbine at a constant tip speed ratio rather than a constant rotational speed. Next, the presence of the drag and the non-linearity of the lift force due to the large excursion in the angles of attack which lead to flow separation, accounts for a further 6% reduction in the power coefficient. Finally, the unsteady effects (load hysteresis, stall delay and dynamic stall) lead to an additional 0.5% reduction. We can then conclude that unsteady phenomena have a small effect on the mean values, whose reduction in unsteady flow conditions is largely due to flow separation.

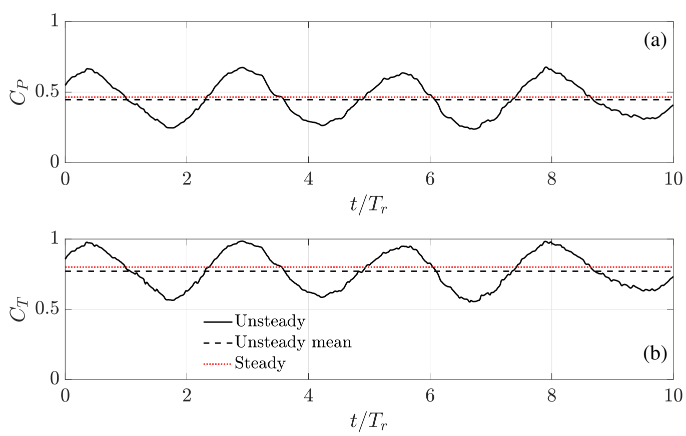

Figure 14: Comparison of (a) power coefficient and (b) thrust coefficient over 10 blade rotations, showing the predicted unsteady time history, and corresponding mean value alongside steady state response.

8.2. Root and edgewise bending moments

Time histories for the blade root (C_{My}) and edgewise (C_{Mx}) bending moment coefficients are shown in Figures 15(a) and 15(b), respectively for the unsteady, steady and quasi-steady predictions. The mean unsteady predictions for C_{My} and C_{Mx} are reduced by 4.5% and 3%, respectively from the steady value and the fluctuations were found to exceed these by 45% and 65%, respectively. The unsteady and quasi-steady time histories have similar periodicity, however, a phase lag and on the most part, an amplitude reduction from the quasi-steady prediction is found. The mean values predicted by the quasi-steady model for both coefficients are within 1% of the unsteady mean, which suggests that a quasi-steady assumption would be reasonable. However, it is important to note that the difference between the standard deviations is 15% higher for C_{My} and 5% for C_{Mx}. Thus the fatigue loads are moderately overpredicted using a quasi-steady approximation.

It is evident that large waves such as those considered here lead to large unsteady variations in the power, thrust and bending moment coefficients. However, there is little effect on the time averaged performance.

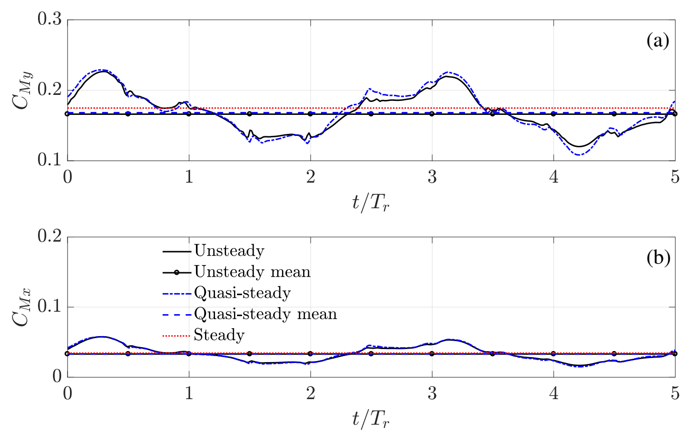

Figure 15: Blade bending moment time histories for (a) root bending and (b) edgewise bending shown over 5 blade rotations for steady, quasi-steady and unsteady predictions.

8.3. Time averaged sectional parameters

We investigate the difference between the unsteady and steady rotor performance by plotting the time averaged axial ($\bar{a}$) and tangential ($\bar{a}'$) induction factors along the blade span in Figures 16(a) and 16(b), respectively for the steady, quasi-steady and unsteady prediction. Firstly, there is no discernible difference between the unsteady and quasi-steady values anywhere along the blade, for either induction factor. Comparing the unsteady and steady predictions, a visible difference is evident inward from approximately $0.4R$ towards the root of the blade, where the steady value is larger for both factors. There is very little difference in the factors at the outer blade sections towards the tip, steady $\bar{a}$ is slightly larger and steady $\bar{a}'$ slightly smaller. Since the majority of the power is generated near the tip, the observed differences in C_P, C_T, C_{Mx}, and C_{My} from the steady state are not fully accounted for by the differences in $\bar{a}$ and $\bar{a}'$.

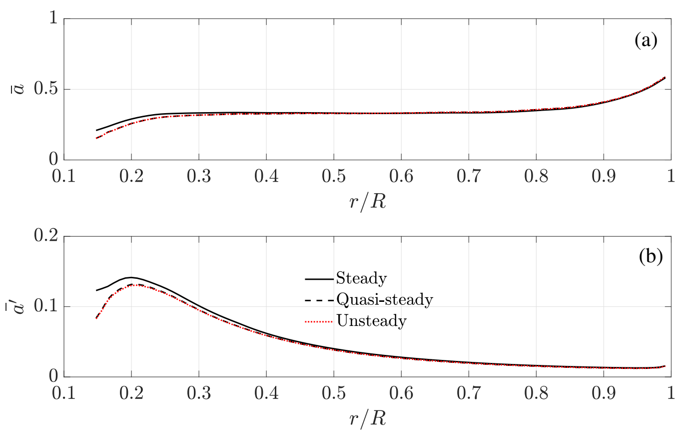

Figure 16: Time averaged (a) axial and (b) tangential induction factors along the blade span for steady, quasi-steady and unsteady predictions.

Time averaged, sectional values for lift ($\bar{C_L}$), drag ($\bar{C_D}$), thrust ($\bar{C_T}$) and torque ($\bar{C_Q}$) coefficients are shown in Figures 17(a- d), respectively, for the steady, quasi-steady and unsteady predictions. The quasi-steady values are determined using static wind tunnel data [29].

Inspecting Figure 17(a) the steady value of $\bar{C_L}$ is greater at the outer sections, where the flow is attached and lower at the inner sections where separation occurs, compared with the unsteady prediction. An increase in both the unsteady and quasi-steady value of $\bar{C_D}$ occurs near the blade root where the flow is highly separated, which will be discussed in the following section. However, from about $0.3R$, $\bar{C_D}$ follows the steady value. As a consequence of the difference in $\bar{C_L}$, the unsteady value of $\bar{C_T}$ is reduced at the outer blade sections, which compounded with the higher dynamic pressure and longer moment arm at the tip, reduces the mean rotor thrust load. Likewise, unsteady $\bar{C_Q}$ is less

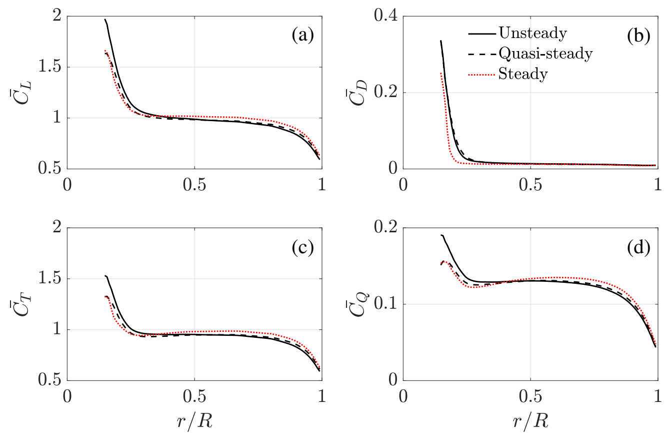

Figure 17: Comparison of mean (a) lift coefficient, (b) drag coefficient, (c) thrust coefficient and (d) torque coefficient along the blade span for steady, quasi-steady and unsteady conditions.

from about $0.3R$ to R than in steady conditions, reducing the mean C_P value.

8.4. Unsteady flow along the blade span

Time histories for f, α and C_L are shown in Figure 18 at locations $0.15R$, $0.4R$ and $0.96R$ on the blade.

Near the tip ($0.96R$), the separation point is a constant and equal to unity, indicating that no separation occurs, which is confirmed by the moderate α fluctuations, which remain inside the attached flow region (-8° to 8°). The associated unsteady C_L is slightly below the quasi-steady value due to the shedding of vorticity from the trailing-edge, which causes a phase lag and amplitude reduction. At the mid-section ($0.4R$) the flow remains attached under steady and unsteady conditions. Moderate separation is evident for the quasi-steady case. The unsteady value of α is in excess of 8°. However, unsteady phenomena reduces the adverse pressure gradient in the boundary layer, causing a delay in separation from the quasi-steady value [41]. The separation point near the blade root ($0.15R$) is a constant 0.7 under steady conditions. The unsteady mean value and amplitude for f is less than the quasi-steady value, indicating that highly non-linear phenomena are occurring. The α history shows that the oscillations

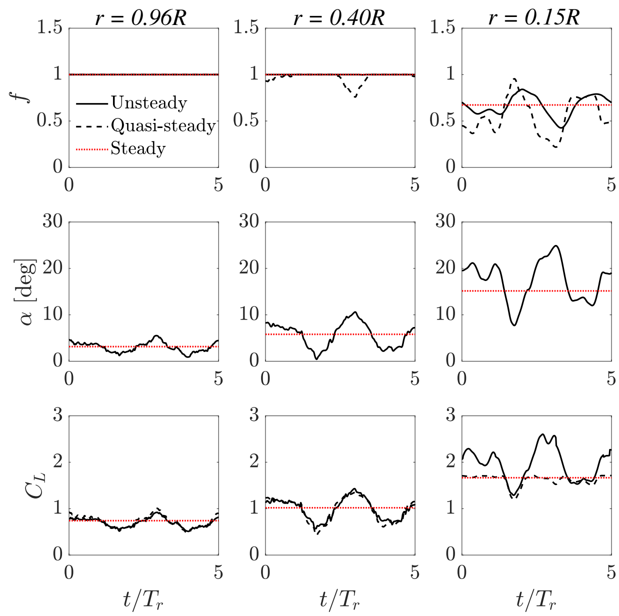

Figure 18: Time histories for separation point, angle of attack and lift coefficient at blade sections near the tip ($r = 0.96R$), mid-section ($r = 0.40R$) and root ($r = 0.15R$).

are almost completely outside of the linear region. The instantaneous C_L computed with the unsteady approach was up to 98% and 71% greater than that computed with a quasi-steady and a steady approach, respectively. The large unsteady C_L value is due to the formation and shedding of the leading-edge vortex.

Relationships between α, C_L and C_D are shown at the tip, mid-section and root in Figure 19 over one wave period (10 s). These plots show the nature of the hysteresis, which is mild at the tip where $k_r \approx 0.02$ where the flow is attached, the amplitude grows as we travel towards the middle of the blade where $k_r \approx 0.1$, hysteresis is not visible in C_L. However, it is evident in C_D. Moving toward the root, the flow is highly unsteady, $k_r \approx 0.3$ and the hysteresis is distinct. This large increase in the C_L above the quasi-steady value is caused by a vortex shedding from the leading-edge.

The build-up and transit of the leading-edge vortex as predicted by the

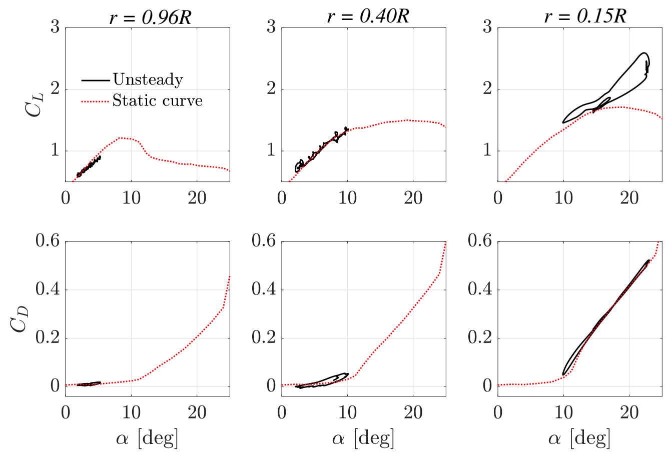

Figure 19: Unsteady lift and drag coefficients with angle of attack for locations near the tip ($r = 0.96R$), mid-section ($r = 0.40R$) and root ($r = 0.15R$) of the blade.

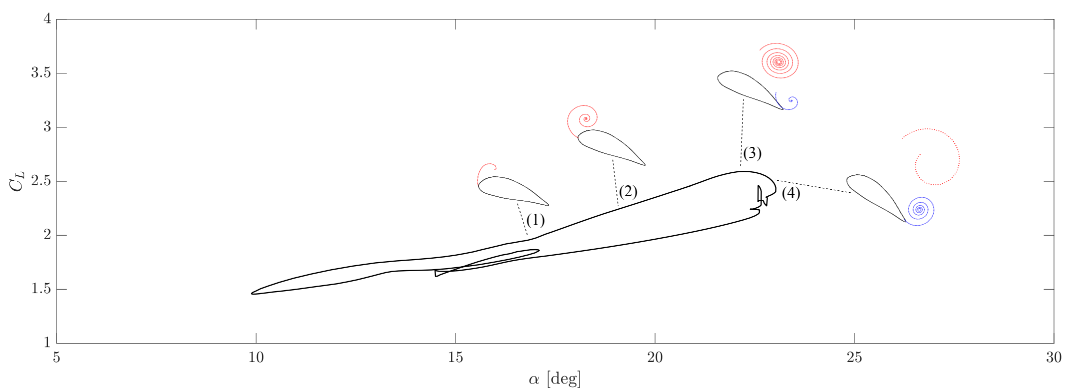

Figure 20: Lift coefficient hysteresis near the blade root showing the stages of leading-edge vortex formation and convection.

model is illustrated in Figure 20 for the blade root section ($r = 0.15R$). At stage 1, $\alpha' > \alpha_{cr}$ inducing leading-edge separation, and initialising the vortex time parameter τ. At stage 2, α has increased causing a build-up in circulation at the leading-edge. At stage 3, the circulation has built up into a concentrated vortex which sheds and convects downstream resulting in a maximum vale of C_L when the vortex is directly above the centre of the foil, in addition a counter circulation has forming at the trailing-edge. At stage 4, $\tau = T_v$, and the leading edge vortex passes the trailing edge and breaks down; concurrently the trailing edge vortex sheds inducing full stall.

The location and duration of separation occurring on the blade is highly dependent on unsteady and rotational effects. In Figure 21 the locations along the blade where separation occurs for (a) the rotational unsteady case, (b) the non-rotating unsteady case and (c) the rotational quasi-steady prediction. The contours represent the percentage of time that separation occurred. For the unsteady rotational case separation is mostly restricted to the very root of the blade where a minimum $f \approx 0.5$ occurs roughly 10% of the time. Significantly, full separation does not occur. For the unsteady non-rotating case separation is also confined to root sections. However, the point of separation moves closer to the leading edge with full separation almost occurring up to 30% of the time. For the quasi-steady prediction we observe that separation occurs over a greater portion of the blade, albeit near the trailing edge. Since the flow is mostly

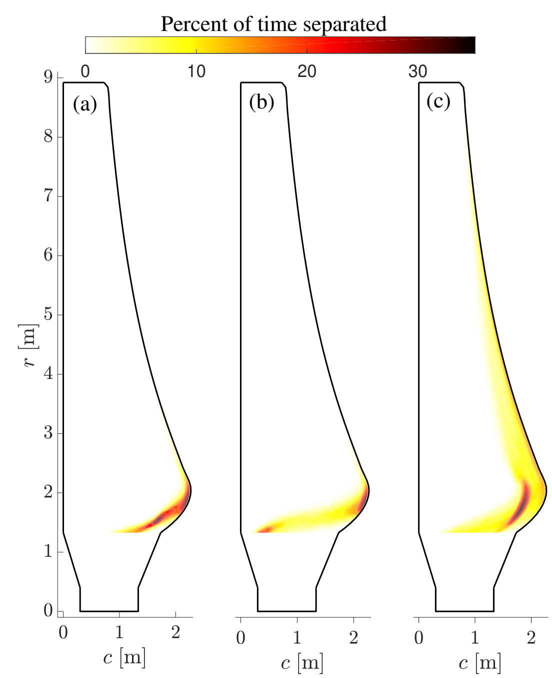

Figure 21: Location and duration in percentage of separation occurring along the blade span for (a) including unsteady and rotational, (b) only unsteady and (c) quasi-steady with rotation.

attached over the blade, there is an overall amplitude reduction from the quasi-steady lift value (Theodorsen's theory). Which explains the reduced standard deviations for the root and edgewise bending moment coefficients compared to the quasi-steady prediction (see Root and edgewise bending moments, Section 8.2). The large overshoots occurring near the root, where the flow is heavily separated has a negligible effect due to the short moment arm, and lower relative velocity.

8.5. Sub-optimal operating conditions

The analysis so far has assumed that the optimal $\lambda = 4.5$ is always met. However, in reality, it will be difficult for the rotor to always rotate at the optimum speed to match the time dependent inflow. In this section we investigate how the flow along the blade span and root bending moment coefficient are effected by a reduced rotor speed causing $\lambda = 4$ and $\lambda = 3.5$, where the the pitch angle which yields maximum C_P for each is $\beta_p = 0.2°$ and $\beta_p = 1.2°$, respectively. In Figures 22(a) and 22(b) the cases of $\lambda = 4$ and $\lambda = 3.5$ are shown, respectively, over 10 periods of revolution. For $\lambda = 4$ we observe a clear difference in the phase and peak values where the quasi-steady prediction was found to be as much as 30% below the unsteady fluctuating value throughout the full time series. There is also a small 2% reduction in the quasi-steady mean value. For the $\lambda = 3.5$ case, the quasi-steady prediction is very poor. A maximum difference of 80% from the unsteady value occurs and the mean value is underpredicted by 8% which is significant.

The quasi-steady prediction is poor at lower values of λ because the flow around the blade undergoes large periods of separation. Shown in Figure 23 is the unsteady prediction (a) and the quasi-prediction (b). Clearly the flow is largely separated over most of the blade span for the unsteady case, thus dynamic stall is also occurring at most span locations, and moreover, the model predicts vortex shedding all the way up from the root to $0.5R$ of the span. Because a large proportion of the blade is undergoing dynamic stall, unlike the optimum $\lambda = 4.5$ case, there is a global effect which causes the peaks in C_{M_y}

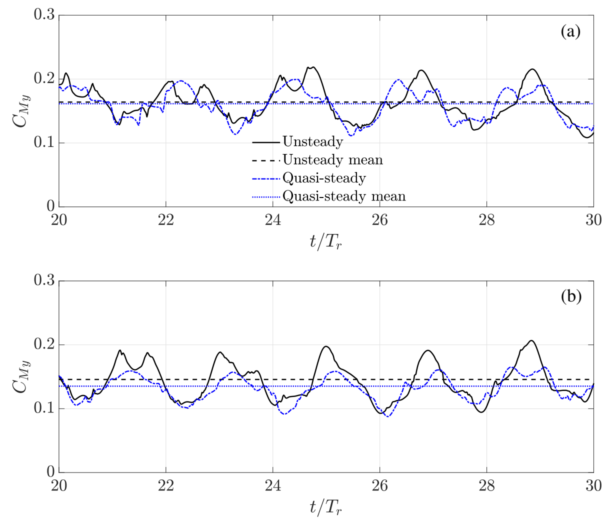

Figure 22: Root bending moment coefficient for (a) tip-speed ratio $\lambda = 4$ and (b) $\lambda = 3.5$.

shown in Figure 22(b). For the quasi-steady prediction separation occurs over almost the entire span, and at some mid-span locations the flow is observed to be approximately two thirds separated ($f \approx 0.33$) for 10% of the time.

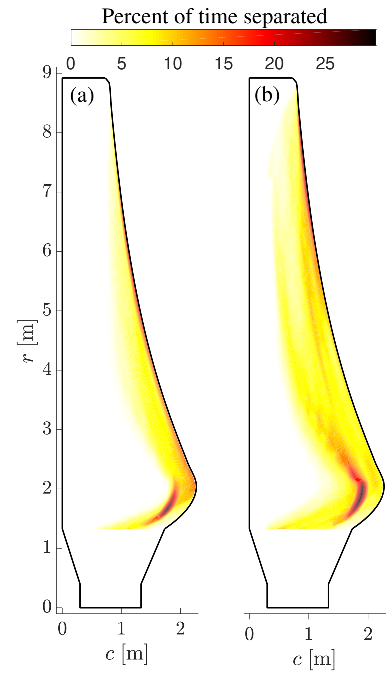

Figure 23: Location and duration in percentage of separation occurring along the blade span for (a) unsteady and (b) quasi-steady predictions.

9. Conclusions

A code based on simple models has been developed to study the unsteady loads of tidal turbines. The code accounts for load hysteresis, dynamic stall, leading-edge vortex shedding and rotational augmentation. The induction factors are computed with blade-element momentum theory, based on a running average of the loads from the previous period of revolution. The code is freely available for use and can be downloaded from our GitHub repository [14].

The onset flow conditions were determined using velocity measurements made at the EMEC test site, where the mean current was 2.72 ms^{-1}. The waves have a characteristic height of approximately 5 m, steepness of 0.17 and a dominant frequency of 0.095 Hz. We modelled an 18 m diameter axial-flow turbine with the hub at a water depth of 27 m. In the first instance, we considered the rotor to operate at a constant, optimal tip-speed ratio of 4.5.

We found that the unsteady loads are governed by the frequency of the waves, and not by the rotational frequency of the turbine. At the outer blade sections, the flow is attached and unsteady phenomena results in a reduction of the mean sectional lift. Towards the mid-section, a delay in flow separation occurs. Near the blade root, dynamic stall and leading-edge vortex shedding cause a twofold increase of the sectional lift compared to the static value. Overall, fluctuations in the root bending moment and power were found to exceed the steady values by almost 50%.

The mean power and thrust, as well as the mean root and edgewise bending moments, show a moderate reduction of less than 5% compared to the steady state. This is largely due to flow separation. However, both the fact that the rotor is operating at fixed rotational speed, and unsteady phenomena, occurring near the tip, make a minor contribution. The extreme loads predicted near the blade root caused by dynamic stall have little effect on the global thrust and torque acting on the blade due to the short lever arm and lower relative flow velocity compared to the outer sections. These results show that large waves induce significant load fluctuations. However, there is little effect on the mean loads and performances of the turbine.

Non-linear unsteady effects on the computation of the induction factors are small, and the difference with using a simple quasi-steady approach is negligible. Similarly, the mean unsteady forces and bending moments computed with the unsteady model are within ca. 1% of those predicted using a quasi-steady approximation. However, the standard deviation of the root and edgewise bending moments are overpredicted by 15% and 5%, respectively. This is due to lift amplitude reduction (Theodorsen's theory), which occurs under unsteady attached flow conditions. Under these optimal operating conditions, a reasonable quasi-steady approximation of the unsteady loadings can be achieved. These findings agree with Galloway *et al*. [9] who determined that dynamic stall may be neglected. However, reducing the rotor speed, such that the turbine operates at sub-optimum tip-speed ratios, increases flow separation and dynamic stall occurs over most of the blade. This concurs with the findings of Milne *et al*. [7]

who showed that dynamic stall can dominate the blade loading at lower tip-speed ratios. At a tip-speed ratio of 3.5, the maximum root bending moment coefficient was almost twice that predicted using a quasi-steady approximation. Clearly, load fluctuations are significantly under-predicted by the quasi-steady approach in this region.

10. Acknowledgements

The first named author is supported by an Engineering and Physical Sciences Research Council studentship. Field measurements were acquired under the ReDAPT project (2010-2015) which was co-funded by the Energy Technologies Institute, UK.

References

References

[1] Neill SP, Vögler A, Goward-Brown AJ, Baston S, Lewis MJ, Gillibrand PA, et al. The wave and tidal resource of Scotland. Renewable Energy 2017;114:3–17. doi:10.1016/j.renene.2017.03.027.

[2] Adcock TAA, Draper S, Houlsby GT, Borthwick AGL, Serhadlioglu S. The available power from tidal stream turbines in the Pentland Firth. Proceedings of the Royal Society A: Mathematical, Physical and Engineering Sciences 2013;469(2157):20130072–. URL: http://rspa.royalsocietypublishing.org/content/469/2157/20130072.shorthttp://rspa.royalsocietypublishing.org/cgi/doi/10.1098/rspa.2013.0072. doi:10.1098/rspa.2013.0072.

[3] Chen L, Lam WH. A review of survivability and remedial actions of tidal current turbines. Renewable and Sustainable Energy Reviews 2015;43:891–900. URL: 10.1016/j.rser.2014.11.071http://linkinghub.elsevier.com/retrieve/pii/S1364032114010107. doi:10.1016/j.rser.2014.11.071.

[4] McCroskey W. Vortex wakes of rotorcraft. In: 33rd Aerospace Sciences Meeting and Exhibit. Reston, Virigina: American Institute of Aeronautics and Astronautics; 1995,URL: http://arc.aiaa.org/doi/10.2514/6.1995-530. doi:10.2514/6.1995-530.

[5] Delorm TM, Zappala D, Tavner PJ. Tidal stream device reliability comparison models. Proceedings of the Institution of Mechanical Engineers, Part O: Journal of Risk and Reliability 2012;226(1):6–17. URL: http://pio.sagepub.com/lookup/doi/10.1177/1748006X11422620. doi:10.1177/1748006X11422620.

[6] DNV-GL . SE-0163 Certification of tidal turbines and arrays. Tech. Rep.; 2015. URL: https://rules.dnvgl.com/docs/pdf/DNVGL/ST/2015-10/DNVGL-ST-0164.pdf.

[7] Milne IA, Day AH, Sharma RN, Flay RGJ. Blade loads on tidal turbines in planar oscillatory flow. Ocean Engineering 2013;60:163–74. URL: http://linkinghub.elsevier.com/retrieve/pii/S0029801812004465. doi:10.1016/j.oceaneng.2012.12.027.

[8] Milne IA, Day AH, Sharma RN, Flay RGJ. The characterisation of the hydrodynamic loads on tidal turbines due to turbulence. Renewable and Sustainable Energy Reviews 2016;56:851–64. URL: http://linkinghub.elsevier.com/retrieve/pii/S1364032115013623. doi:10.1016/j.rser.2015.11.095.

[9] Galloway PW, Myers LE, Bahaj AS. Quantifying wave and yaw effects on a scale tidal stream turbine. Renewable Energy 2014;63:297–307. URL: http://www.sciencedirect.com/science/article/pii/S0960148113004977. doi:10.1016/j.renene.2013.09.030.

[10] Butterfield CP, Hansen AC, Simms D, Scott G. Dynamic stall on wind turbine blades. Tech. Rep.; National Renewable Energy Lab., Golden, CO (United States); 1991.

[11] Tully S, Viola IM. Reducing the wave induced loading of tidal turbine blades through the use of a flexible blade. International Symposium on Transport Phenomena and Dynamics of Rotating Machinery (ISROMAC 2016) 2016;:9.

[12] Young AM, Farman JR, Miller RJ. Load alleviation technology for extending life in tidal turbines. In: Progress in Renewable Energies Offshore-Proceedings of 2nd International Conference on Renewable Energies Offshore, RENEW 2016. 2016, p. 521–30.

[13] Energy Technologies Institute . ReDAPT MC7.3 public domain report. Tech. Rep.; 2015.

[14] Scarlett GT, Viola IM. Tidal turbine hydrodynamic model. 2017. URL: https://github.com/gabscarlett.

[15] UKERC . Energy Data Centre. 2018. URL: http://data.ukedc.rl.ac.uk/simplebrowse.

[16] Sellar B, Wakelam G, Sutherland DRJ, Ingram DM, Venugopal V. Characterisation of tidal flows at the European marine energy centre in the absence of ocean waves. Energies 2018;11(1):176. URL: http://www.mdpi.com/1996-1073/11/1/176. doi:10.3390/en11010176.

[17] Gretton GI. Development of a computational fluid dynamics model for a horizontal axis tidal current turbine. Tech. Rep. WG3 WP5 D1; 2010.

[18] Sheng W, Galbraith RAM, Coton FN. Applications of low-speed dynamic-stall model to the NREL airfoils. Journal of Solar Energy Engineering 2010;132(1):011006. URL: http://solarenergyengineering.asmedigitalcollection.asme.org/article.aspx?articleid=1473733. doi:10.1115/1.4000329.

[19] Burton T, Jenkins N, Sharpe D, Bossanyi E. Wind Energy Handbook. Chichester, UK: John Wiley & Sons, Ltd; 2011. ISBN

9781119992714. URL: http://doi.wiley.com/10.1002/9781119992714. doi:10.1002/9781119992714.

[20] Buhl ML. A new empirical relationship between thrust coefficient and induction factor for the turbulent windmill state. Tech. Rep. August; 2005.

[21] Ning AS. A simple solution method for the blade element momentum equations with guaranteed convergence. Wind Energy 2014;17:1327–45. URL: http://onlinelibrary.wiley.com/doi/10.1002/we.1608/fullhttp://doi.wiley.com/10.1002/we.1636. doi:10.1002/we.1636. arXiv:arXiv:1006.4405v1.

[22] Sheng W, Galbraith RAM, Coton FN. A modified dynamic stall model for low Mach numbers. Journal of Solar Energy Engineering 2008;130(3):031013. URL: http://dx.doi.org/10.1115/1.2931509http://solarenergyengineering.asmedigitalcollection.asme.org/article.aspx?articleid=1474262. doi:10.1115/1.2931509.

[23] Beddoes TS. A third generation model for unsteady aerodynamics and dynamic stall. Tech. Rep.; Westland Helicopters Limited; 1993.

[24] Hansen MH, Gaunaa M, Madsen HA. A Beddoes-Leishman type dynamic stall model in state-space and indicial formulations. Tech. Rep.; 2004. URL: http://www.risoe.dk/rispubl/vea/veapdf/ris-r-1354.pdf.

[25] Theodorsen T. General theory of aerodynamic instability and the mechanism of flutter. NACA Technical Report 496 1935;:413 –33.

[26] Wagner H. Über die entstehung des dynamischen auftriebes von tragflügeln. Journal of Applied Mathematics and Mechanics/Zeitschrift für Angewandte Mathematik und Mechanik 1925;5(1):17–35.

[27] Jones RT. The unsteady lift of a wing of finite aspect ratio. NACA Report 681 1940;doi:10.1017/CBO9781107415324.004. arXiv:arXiv:1011.1669v3.

[28] Thwaites B. Incompressible Aerodynamics: An account of the theory and observations of the steady flow of incompressible fluid past aerofoils, wings and other bodies. University Oxford Press; 1960.

[29] Janiszewska JM, Reuss Ramsay R, Hoffmann MJ, Gregorek GM. Effects of grit roughness and pitch oscillations on the S814 airfoil. Tech. Rep.; 1996. doi:10.2172/266691.

[30] Sheng W, Galbraith RAM, Coton FN. A new stall-onset criterion for low speed dynamic-stall. Journal of Solar Energy Engineering 2006;128(4):461. URL: http://solarenergyengineering.asmedigitalcollection.asme.org/article.aspx?articleid=1457809. doi:10.1115/1.2346703.

[31] Hansen M, Sørensen J, Voutsinas S, Sørensen N, Madsen H. State of the art in wind turbine aerodynamics and aeroelasticity. Progress in Aerospace Sciences 2006;42(4):285–330. URL: http://linkinghub.elsevier.com/retrieve/pii/S0376042106000649. doi:10.1016/j.paerosci.2006.10.002.

[32] Du Z, Selig M. The effect of rotation on the boundary layer of a wind turbine blade. Renewable Energy 2000;20(2):167–81. URL: http://linkinghub.elsevier.com/retrieve/pii/S0960148199001093. doi:10.1016/S0960-1481(99)00109-3.

[33] Hand MM, Simms Da, Fingersh LJ, Jager DW, Cotrell JR, Schreck S, et al. Unsteady aerodynamics experiment phase VI: wind tunnel test configurations and available data campaigns. Tech. Rep. December; National Renewable Energy Laboratory (NREL); Golden, CO; 2001. URL: http://www.osti.gov/servlets/purl/15000240-1FhaHo/native/. doi:10.2172/15000240.

[34] Breton SP, Coton FN, Moe G. A study on rotational effects and different stall delay models using a prescribed wake vortex scheme and NREL phase VI experiment data. Wind Energy 2008;11(5):459–82. URL: http://doi.wiley.com/10.1002/we.269. doi:10.1002/we.269.

[35] Lindenburg C. Modelling of rotational augmentation based on engineering considerations and measurements. In: European Wind Energy Conference. 2004, p. 22–5.

[36] Viterna L, Corrigan R. Fixed pitch rotor performance of large horizontal axis wind turbines. Tech. Rep.; NASA Lewis Research Center; 1981.

[37] Ning A, Hayman G, Damiani R, Jonkman JM. Development and validation of a new blade element momentum skewed-wake model within AeroDyn. In: 33rd Wind Energy Symposium. December 2014; Reston, Virginia: American Institute of Aeronautics and Astronautics. ISBN 978-1-62410-344-5; 2015,URL: http://www.nrel.gov/docs/fy15osti/63217.pdfhttp://arc.aiaa.org/doi/10.2514/6.2015-0215. doi:10.2514/6.2015-0215.

[38] Guntur S, Sørensen NN, Schreck S, Bergami L. Modeling dynamic stall on wind turbine blades under rotationally augmented flow fields. Wind Energy 2016;19(3):383–97. URL: http://onlinelibrary.wiley.com/doi/10.1002/we.1608/fullhttp://doi.wiley.com/10.1002/we.1839. doi:10.1002/we.1839. arXiv:arXiv:1006.4405v1.

[39] McNaughton J, Harper S, Sinclair R, Sellar B. Measuring and modelling the power curve of a commercial-scale tidal turbine. In: The 11th European Wave and Tidal Energy Conference. 2015, p. 1–9.

[40] Scarlett G, Viola IM. Unsteady tidal turbine blade loading: an analytical approach. In: 5th Oxford Tidal Energy Workshop. April; 2016, p. 26–7.

[41] Ericsson L, Reding J. Fluid mechanics of dynamic stall part I. Unsteady flow concepts. Journal of Fluids and Structures 1988;2(1):1–33. URL: http://linkinghub.elsevier.com/retrieve/pii/S0889974688901168. doi:10.1016/S0889-9746(88)90116-8.